

## **Novel Fe-Mn-Si-Pd alloys: insights on mechanical, magnetic, corrosion and biocompatibility performance**

Yu Ping Feng,<sup>a</sup> Andreu Blanquer,<sup>b</sup> Jordina Fornell,<sup>\*a</sup> Huiyan Zhang,<sup>a</sup> Pau Solsona,<sup>a</sup> Maria Dolores Baró,<sup>a</sup> Santiago Suriñach,<sup>a</sup> Elena Ibáñez,<sup>b</sup> Eva García-Lecina,<sup>c</sup> Xinquan Wei,<sup>d</sup> Ran Li,<sup>d</sup> Lleonard Barrios,<sup>b</sup> Eva Pellicer,<sup>a</sup> Carme Nogués<sup>b</sup> and Jordi Sort<sup>a,e</sup>

*<sup>a</sup>Departament de Física, Universitat Autònoma de Barcelona, E-08193 Bellaterra, Spain*

*<sup>b</sup>Departament de Biologia Cel·lular, Fisiologia i Immunologia, Universitat Autònoma de Barcelona, E-08193 Bellaterra, Spain*

*<sup>c</sup>Surfaces Division, IK4-CIDETEC, Parque Tecnológico de San Sebastián, E-20009 Donostia, Spain*

*<sup>d</sup>Key Laboratory of Aerospace Materials and Performance, School of Materials Science and Engineering, Beihang University, 100191 Beijing, China*

*<sup>e</sup>Institució Catalana de Recerca i Estudis Avançats (ICREA), Passeig Lluís Companys 23, E-08010 Barcelona, Spain*

*\*Corresponding author. E-mail address: jordina.fornell@uab.cat*

## ABSTRACT

Two new Fe-based alloys, Fe-10Mn6Si1Pd and Fe-30Mn6Si1Pd, have been fabricated by arc-melting followed by copper mold suction casting. The Fe-30Mn6Si1Pd alloy mainly consists of  $\epsilon$ -martensite and  $\gamma$ -austenite Fe-rich phases whereas the Fe-10Mn6Si1Pd alloy primarily contains  $\alpha$ -Fe(Mn)-ferrite phase. Additionally, Pd-rich precipitates were detected in both alloys. Good mechanical response was observed by nanoindentation: hardness values around 5.6 GPa and 4.2 GPa and reduced Young's modulus values of 125 GPa and 93 GPa were measured for the as-prepared Fe-10Mn6Si1Pd and Fe-30Mn6Si1Pd alloys, respectively. Both alloys are thus harder and exhibit lower Young's modulus than 316L stainless steel, which is one of the most common Fe-based reference materials for biomedical applications. Compared with the ferromagnetic Fe-10Mn6Si1Pd alloy, the paramagnetic Fe-30Mn6Si1Pd alloy is more appropriate to be used as an implant since it would be compatible with nuclear magnetic resonance (NMR) and magnetic resonance imaging (MRI) analyses. Concerning biocompatibility, the more hydrophilic Fe-10Mn6Si1Pd shows improved cell adhesion but its pronounced ion leaching has a negative effect on the proliferation of cells. The influence of immersion in simulated body fluid on composition, microstructure, mechanical and magnetic properties of both alloys is assessed, and the correlation between microstructure evolution and physical properties is discussed.

## 1. Introduction

Over the past few years, the interest in novel permanent and biodegradable metallic alloys has been continuously increasing. While Ti alloys have established as the ideal materials for permanent orthopaedic implants, Mg-based and Fe-based alloys are considered potential candidates to be used as temporary medical biodegradable implants, such as stents or bone replacements.<sup>1-5</sup> The main advantage of biodegradable implants, compared with permanent ones, is that a secondary surgery for implant removal can be avoided, improving the patient's comfort and reducing the cost of medical treatment. Mg and its alloys are free from toxic elements, and exhibit fast biodegradability and a Young's modulus closer to that of the human bone. However, the high degradation rates of Mg alloys may limit their use in certain applications where the implant needs to stay in the body for at least a specific period of time. Furthermore, the accompanying considerable amounts of hydrogen release could impede a good connectivity between osteocytes and the alloy. Also, for some applications, the strength and ductility of Mg-alloys are not good enough for supporting our body.<sup>3,6</sup>

Recently, because of the good preliminary results obtained in *in-vitro* and *in-vivo* experiments, attention is being paid to Fe-based alloys.<sup>7,8</sup> However, the degradation rate of most Fe-based alloys is still too low to meet the requirements of degradable stent applications.<sup>3</sup> In addition, some Fe-based alloys are ferromagnetic, thus precluding their use in specific usages where nuclear magnetic resonance (NMR) or magnetic resonance imaging (MRI) analyses are required to monitor the patient's recovery after surgery.

During the last few years, FeMn,<sup>3,9-12</sup> FeMnPd<sup>3,9</sup> and FeMnSi<sup>13</sup> alloys with enhanced degradation rates and mechanical properties similar to those of 316L stainless steel have been manufactured for stent materials. The addition of Mn within the solubility limit of Fe reduces the standard electrode potential of Fe to make it more susceptible to corrosion.<sup>3,9-12</sup> The addition of noble alloying elements, such as Pd, can generate small and homogeneously dispersed Pd-rich precipitates that act as cathodic sites to induce microgalvanic corrosion.<sup>3</sup> Previous studies have shown that silicon addition to Fe-30Mn alloy increases its corrosion rate. This fact has been attributed to larger  $\gamma$ -austenite contents, which corrodes faster than  $\epsilon$ -martensite, in the alloys containing silicon.<sup>13</sup> Moreover, the tensile strength increases significantly with the increase of Si

content in the Fe-Mn-Si alloy.<sup>13,14</sup> Besides, some Fe-Mn-Si alloys have been studied for a long time<sup>13,15</sup> because of their shape memory behavior, which may also be of interest for some applications in the biomedical field (e.g., stents).<sup>13</sup> With the appropriate transformation temperature and microstructure, these ternary alloys might be used as self-expandable stents taking advantage of the superelasticity effect, thus minimizing the risk of damaging the vascular tissue due to inflammation reactions produced by the balloon expansion in conventional stenting procedures using non-superelastic materials.<sup>16</sup>

The goal of this work is to obtain suitable Fe-based alloys with improved properties to be used in biomedical applications. With this purpose, two different compositions have been designed. On the one side, the addition of 1wt.% of Pd to the ternary Fe-30Mn-6Si is expected to increase its degradation rate because of the formation of small and homogeneously dispersed Pd-rich precipitates. On the other side, the addition of 6 wt.% of Si to the ternary Fe-10Mn-1Pd, besides increasing the strength of the alloy, is expected to aid the healing process and to help the immunologic system, as silicon is an essential mineral in the human body.<sup>13</sup> So far only the binary and ternary alloys have been investigated and hence, the idea of our work is to produce a quaternary alloys that take advantage of all the aforementioned properties in a synergetic way. In the present manuscript, two newly developed Fe-10Mn6Si1Pd and Fe-30Mn6Si1Pd have been fabricated by arc-melting and copper-mold suction casting and their properties (magnetic, mechanical, corrosion resistance, wettability and biocompatibility) have been characterized. The use of this synthetic approach allows obtaining homogenous Fe-based alloys with Pd-rich precipitates and competitive properties compared to the up-to-date reported Fe-based materials.

While the Fe-10Mn6Si1Pd alloy is ferromagnetic, Fe-30Mn6Si1Pd remains non-magnetic both in the as-cast state and after short- and long-term immersion tests in Hank's solution. The evolution of microstructure and mechanical properties during the course of immersion experiments has been also assessed. From the biological point of view, two different parameters have been analyzed: cytotoxicity, which allows determining whether the partial dissolution of the alloy produces a decrease in the cell number with time; and proliferation, which enables to determine not only if the alloy causes cytotoxicity, but also if cells can divide and proliferate (increase of their number over time).

## 2. Materials and methods

### 2.1. Materials

Commercial Fe (97%), Si (99%), Mn (99%) and Pd (99.95%) were mechanically milled in a shaker mill device (SPEX 8000 M) at room temperature, with a nominal composition of Fe-10Mn6Si1Pd and Fe-30Mn6Si1Pd (wt.%). The powders were milled under Ar atmosphere in a ball-to-powder weight ratio of 1:1 for 15 h. All the operations prior to milling (weighting of the powder and sealing of the container) were done in a glove box under Ar atmosphere (<0.2 O<sub>2</sub> ppm, <0.1 H<sub>2</sub>O ppm) to avoid oxidation or any other atmospheric contamination. Subsequently, the powders were consolidated by a uniaxial cold press under a pressure of 100 MPa to obtain disks of approximately 5 mm in thickness. Then, the disks were melted in a mini arc-melting furnace (MAM1, Edmund Bühler Lab Tec) under Ar atmosphere and suction casted into a copper mold to produce cylindrical rods of 3 mm in diameter and a few centimeters in length. The same procedure was used to produce a control Pd-free alloy for corrosion experiments with a nominal composition of Fe-30Mn-6Si.

The real compositions of the as-cast rods, as measured by energy dispersive X-ray spectroscopy (EDX), were Fe-9.97Mn-5.71Si1.19Pd and Fe-29.17Mn5.76Si1.26Pd (wt.%).

### 2.2. Immersion tests

Prior to immersion tests, pieces of 3 mm in diameter and 1 mm thickness of the as-cast alloys were cold-embedded in epoxy resin and ground up to P4000 grit with SiC. The alloys were then immersed in 28 ml of Hank's balanced salt solution at 37±1 °C for different times, up to 120 days. The volume of solution was selected to conform with the ASTM-G31-72 norm.<sup>17</sup> Hank's balanced salt solution (HBSS) is a widely used simulated physiological fluid to reproduce in vivo conditions.<sup>13,18,25</sup> After immersion, the samples were removed from Hank's solution, rinsed with alcohol, and dried in air. The microstructure, mechanical properties and magnetic behavior were subsequently assessed as a function of immersion time. Also, 3 ml of Hank's solution were pipeted off to measure the ion released concentration of Fe, Mn, Si and Pd by inductively coupled plasma optical emission spectroscopy (ICP-OES). In parallel, alloys were also immersed in 1 ml

of Dulbecco's Modified Eagle's Medium (DMEM, Gibco) with 10% foetal bovine serum (FBS, Gibco) and incubated under standard conditions (37°C and 5% CO<sub>2</sub>) for different times, to measure ion release by ICP-OES in exactly the same conditions as for the cell cultures. In order to ensure the tests are reproducible, three replicates were prepared and analyzed per sample.

### ***2.3. Structural Characterization***

Scanning electron microscopy (SEM) using a Zeiss Merlin microscope equipped with energy dispersive X-ray spectroscopy (EDX) was used for morphological and compositional analyses. X-ray diffraction (XRD) was carried out using a Philips X'Pert diffractometer with Cu K $\alpha$  radiation. Measurements were performed in the angular range 25-100° with a step size of 0.04°. Differential scanning calorimetry (DSC) (Perkin Elmer, DSC 8000) was used to detect the austenite to martensite phase transformation in the alloy with 30 wt. % of Mn.

### ***2.4. Characterization of the physical and mechanical properties***

Nanoindentation measurements were carried out in the as-cast and immersed samples using a UMIS nanoindenter from Fischer-Cripps Laboratories, with a Berkovich pyramidal-shaped diamond indenter. Prior to nanoindentation, the as-cast samples were polished to mirror-like appearance using in the final step 1 $\mu$ m diamond particles solution. The roughness of the as-cast samples was measured with a Leica DCM 3D system that combines confocal and interferometry technologies. The maximum applied load in nanoindentation tests was 500 mN. The results were averaged over more than 20 indents to obtain statistically reliable data. The Berkovich hardness ( $H$ ) and reduced Young's modulus ( $E_r$ ) values were evaluated from the load-displacement curves at the beginning of the unloading segments, using the method of Oliver and Pharr.<sup>20</sup> Compression tests were carried out in cylinder-shaped samples with an aspect ratio (length:diameter) of 2:1 at a strain rate of  $2 \times 10^{-4} \text{ s}^{-1}$  using an equipment from MTS (CMT5105, 100kN). Hysteresis loops were collected using a vibrating sample magnetometer (VSM) from Oxford Instruments, with a maximum applied magnetic field of 12 kOe at room temperature.

## ***2.5. Electrochemical potentiodynamic polarization measurements and wettability***

The corrosion behavior of the as-cast alloys was evaluated by potentiodynamic polarization, which was carried out in a single compartment, double-walled cell with a typical three-electrode configuration (connected to an Autolab 302N potentiostat/galvanostat) at  $37 \pm 1$  °C in Hank's solution, analogous to the configuration we previously used for Ti-based biomaterials.<sup>21</sup> A double junction Ag/AgCl with 3 M KCl inner solution and 1 M NaCl outer solution was used as the reference electrode while a Pt sheet was used as the counter electrode. Prior to the measurements, the specimens were immersed in the electrolyte for 1 h to obtain the open circuit potential (OCP). Three samples of each composition were measured to prove good repeatability. The upper and lower potential limits were set at  $-300$  mV and  $+1500$  mV with respect to the OCP. The scan rate was  $0.5$  mV/s.

To assess the wettability, the contact angles were determined by means of the sessile drop technique, using a surface analyzer (CAM 200, Iberlaser). The liquid utilized for the measurements was  $1$   $\mu$ l droplets of Hank's solution at room temperature.

## ***2.6. Cytotoxicity tests and proliferation assays***

Saos-2 human osteosarcoma cells (ATCC) were cultured in DMEM with 10% FBS under standard conditions. To assess cytotoxicity, alloy disks were cleaned with absolute ethanol, introduced into a 4-multiwell culture plate and sterilized by UV light for at least 2 h. Once sterilized, 50,000 cells were seeded into each well and cultured for 1, 3, 7 and 40 days. Cell viability on disk surfaces was evaluated using the Live/Dead Viability/Cytotoxicity kit for mammalian cells (Invitrogen), according to the manufacturer's protocol. Images from different regions of the alloy disk and from the control culture (without disk) were captured using an Olympus IX71 inverted microscope equipped with epifluorescence. For proliferation assay, a total amount of 50,000 Saos-2 cells were seeded into each well of a 4-multiwell plate containing the alloy disk. After 24 h, disks with adhered cells on their surface were transferred to a 96-multiwell plate, and medium with 10% of Alamar Blue (Invitrogen) was added into each well and incubated for 4 h at  $37^\circ\text{C}$  and 5%  $\text{CO}_2$ , protected from direct light. Then, the supernatant was collected and the fluorescence was read using a Cary Eclipse fluorescence spectrophotometer (Agilent Technologies). Cells on the disk were incubated again with fresh medium, and the

Alamar Blue analysis was repeated at 3, 7, 14 and 60 days. Negative controls without cells were also analyzed.

The same samples used for the cytotoxicity and cell proliferation assays were then processed to be observed by SEM. Cultured cells were rinsed twice in phosphate buffered saline (PBS), fixed in 4% paraformaldehyde (PFA, Sigma) in PBS for 45 min at room temperature and rinsed twice in PBS. Cell dehydration was performed in a series of ethanol (50%, 70%, 90% and twice 100%), 7 min each. Finally, samples were dried using hexamethyl disilazane (Electron Microscopy Sciences) for 15 min, mounted on special stubs and analyzed using SEM.

### ***2.7. Hemolysis test***

To evaluate the hemocompatibility of the alloys, 1 cm<sup>2</sup>/ml of Fe<sub>10</sub>MnSiPd and Fe<sub>30</sub>MnSiPd were soaked in 10 ml PBS in centrifuge tubes and kept at 37 °C for 30 min. Then, 0.2 ml of diluted blood (4 ml of human blood in 5 ml PBS) were added to the samples and kept at 37°C for 1 h. Next, tubes were centrifuged at 2500 rpm for 5 min. The supernatant from each tube was transferred to a well of a 24-well plate and the optical density (OD) was recorded in a spectrophotometer at 545 nm wavelength. A negative control (10 ml PBS with 0.2 ml diluted blood) and positive control (10 ml distilled water with 0.2 ml diluted blood) were also recorded. The hemolysis ratio (HR) was calculated according to the equation:  $HR = [(OD_t - OD_n) / (OD_p - OD_n)] \times 100\%$ . The OD<sub>t</sub> is the OD value of the tested group. The OD<sub>n</sub> and OD<sub>p</sub> are the OD values of negative and positive controls, respectively.

## **3. Results and discussion**

### ***3.1. Microstructure and compositional analyses***

#### ***3.1.1. Morphology and crystallographic phase composition of the as-cast alloys***

Figure 1 shows the SEM micrographs (backscattered electrons) of the Fe-10Mn6Si1Pd (panel a) and Fe-30Mn6Si1Pd (panel b) as-cast alloys. Both of them show the typical dendritic morphology: a lighter phase enriched in Fe (according to EDX analysis), embedded in a darker phase slightly enriched in Si and Mn (see Figure 1S in Supporting Information, S.I.). The bright



spots distributed within the darker phase are Pd-rich precipitates (Figure 1S in S.I.). The formation of noble Pd-rich precipitates is expected to induce microgalvanic corrosion, which is supposed to enhance the degradation rate of the alloys. The roughness averages (Ra) of the as-cast samples were 8.04 nm and 6.6 nm for the alloys with 10 and 30 % of Mn, respectively. Figure 1c illustrates the XRD patterns of as-cast Fe-10Mn6Si1Pd and Fe-30Mn6Si1Pd alloys. The alloy with 10 wt.% Mn is composed of  $\alpha$ -Fe (space group Im3m and cell parameter  $a = 2.88 \text{ \AA}$ ). Conversely, the as-cast alloy with 30 wt.% Mn mainly consists of  $\epsilon$ -martensite (P6<sub>3</sub>/mmc,  $a = 2.55 \text{ \AA}$ ,  $c = 4.14 \text{ \AA}$ ), and  $\gamma$ -austenite (Fm3m,  $a = 3.60 \text{ \AA}$ ) phases.

The alloy with 30 wt.% Mn is a shape memory alloy and can exhibit superelasticity or shape memory effect depending on the stable phase at the test temperature. Both alloys were characterized in the as-cast condition without subjecting them to any thermal treatment. Consequently, at room temperature, the alloy with 30% of Mn has a mixed microstructure (austenite and martensite phases) but, by adjusting the testing temperature or subjecting the alloy to an appropriate heat treatment, pure austenite, responsible of superelasticity behavior, or martensite, responsible of shape memory effect, could be obtained. Differential scanning calorimetry (DSC) at 10 K/min was used to identify the transformation temperatures (Figure 2S in S.I.). The austenite finish and start temperatures, and the martensite start and finish temperatures are, respectively:  $A_f \approx 250 \text{ }^\circ\text{C}$ ,  $A_s \approx 150 \text{ }^\circ\text{C}$ ,  $M_s \approx 58 \text{ }^\circ\text{C}$  and  $M_f \approx -30 \text{ }^\circ\text{C}$ . In agreement with DSC measurements and, as evidenced by XRD, the Fe-30Mn6Si1Pd alloy is a mixture of austenite and martensite at room temperature (Figure 1). However, if the alloy was cooled to below  $M_s$ , (i.e.,  $T < -30 \text{ }^\circ\text{C}$ ) and subsequently warmed up to room temperature at open air, the resulting phase would be only martensite and the alloy would exhibit shape memory behavior at room temperature.<sup>22</sup> In the same way, superelasticity would be expected above 250  $^\circ\text{C}$ .<sup>23</sup> Hence, this feature can broaden the application window of this particular alloy.

### ***3.1.2. Surface morphology and chemical analyses as a function of immersion time***

The morphological evolution of both alloys after immersion in Hank's solution for 1 and 4 months is illustrated in Figure 2. After 1 month, two different regions can be distinguished at the surface of the Fe-10Mn6Si1Pd alloy: a rougher region, covered with corrosion products, and a smoother region, free from corrosion products. The partial coverage with the rough layer

indicates that this layer is probably not very well adhered to the surface of the alloy and tends to peel off upon cleaning the sample. Conversely, the alloy with 30% of Mn is completely covered with a well-adhered and considerably smoother oxide layer. Similar trends are observed after 4 months of immersion, i.e., while a rather compact oxide layer covers the surface of the alloy with 30% Mn, a cracked and a peeled off oxide layer can be observed in the alloy with 10% of Mn. These observations reveal that the samples exhibit a characteristic “cracked-earth” appearance which is often encountered in this type of samples after immersion tests and probably caused by dehydration of the degradation layer after removal from the electrolyte.<sup>19,24,25</sup> Further evidence of the poor and good adhesion of the oxide layer for the alloys with 10 and 30% of Mn, respectively, after immersion for one month in Hank’s solution can be observed in the cross section SEM images (Fig. 3). In the Fe-10Mn6Si1Pd alloy it was difficult to find a zone with the oxide layer completely attached to the surface, and the areas where the layer did not peel off were thin and often cracked. Conversely, in the Fe-30Mn6Si1Pd alloy, a compact 3-5  $\mu\text{m}$  thick oxide layer was observed across the entire surface. EDX mappings of both alloys after 1 month of immersion in Hank’s solution revealed that the outermost layer covering the alloys had less amount of Fe and Mn than in the initially bulk material and it was enriched in O and P. Some Ca- rich agglomerates were also detected. Also, in both cases but, most clearly observed in the EDX mapping of the alloy with 30 % of Mn, a Si-rich layer was formed next to the alloy but note that the outermost layer is completely depleted in Si, indicating its fastest degradation.

After 4 months immersion, the thickness of the oxide layer increased ( $\sim 40 \mu\text{m}$  for the alloy with 30 % Mn and  $\sim 12 \mu\text{m}$  for the alloy with 10 % Mn) but in the alloy with 10% of Mn it was still difficult to find a well-adhered corrosion product layer (Figure 3S in the S.I.). The EDX mappings shown in Figure 4 reveal that the oxide layer formed in the Fe-30Mn6Si1Pd alloy is rich in Si and O and it is depleted in Fe and Mn, when compared with the elemental composition of the metallic material underneath. Si is known to be an element prone to oxidation. In fact, in alkaline solutions, the standard reduction potential ( $E^0$ ) for the reaction  $\text{SiO}_3^{2-} + 3\text{H}_2\text{O} + 4\text{e}^- \rightarrow \text{Si} + 6\text{OH}^-$  is -1.69 V. The standard potential for Pd, Fe and Mn are the following ones:  $E^0_{\text{Pd}^{2+}/\text{Pd}} = 0.95\text{V}$ ,  $E^0_{\text{Fe}^{2+}/\text{Fe}} = -0.44 \text{ V}$  and  $E^0_{\text{Mn}^{2+}/\text{Mn}} = -1.18\text{V}$ .<sup>26</sup> Therefore, among all these elements, silicon is the one with the more negative standard potential, thus probably the more prone to be oxidized. Even though kinetics of degradation/corrosion between Fe-30Mn6Si1Pd and Fe-

10Mn6Si1Pd alloys are different, same trends were observed in terms of oxide/hydroxide formation as can be observed in the SEM cross-section image (Figure 4S in the S.I.) of the alloy with 10 % of Mn.

To gain further insight on the corrosion product layers, XRD analyses were carried out on the alloys after 1, 2 and 4 months of immersion in Hank's solution (Figure 5S in the S.I.). The results are in fairly good agreement with SEM observations. No peaks were detected in the alloy with 10 % of Mn as the corrosion product layers were thin and not continuous. Conversely, in the alloy with 30 % of Mn additional peaks belonging to FeO and SiO<sub>2</sub> were observed after 2 and 4 months of immersion.

The amounts of Fe and Mn ions released from the Fe-10Mn6Si1Pd and Fe-30Mn6Si1Pd alloys after immersion in Hank's solution (28 ml) for 7, 30, 60 and 120 days is shown in Figure 5. Larger amounts of the two main elements, Fe and Mn, are released from the alloy with 10 wt. % of Mn even if the initial amount of Mn was lower in this case than for the alloy with 30 % Mn. Therefore, the extraction tests, carried out in accordance with the ASTM-G31-72 standard, clearly reveal a higher degradation rate for this alloy. The Pd concentration was close to the detection limit of the equipment. As a general trend, a sharp increase of ion concentration with immersion time is observed; however, after 60 days, the increase of ion concentrations tends to level off. The parabolic shape of the ion concentration curves has been previously attributed to the formation of degradation products on the alloy's surface. This oxide/hydroxide degradation layer hinders the ion release as the alloy is not in direct contact with media and degradation needs to take place by diffusion of Fe and Mn ions through the layer.<sup>19,25</sup> These results are in good agreement with our SEM observations where thicker and denser degradation layers are observed for the alloy with 30 % of Mn and thinner and looser ones are formed in the alloy with 10 % of Mn. In addition, a drastic reduction in the Fe ion concentration is observed after long-term immersion for the Fe-10Mn6Si1Pd alloy. This was accompanied with the formation of particle precipitates at the bottom of the Hank's solution container, probably in the form of Fe oxides or hydroxides, which were excluded for the ion release analyses. The differences observed between both alloys (i.e. ion release and hydro(oxides) formation) can be mainly attributed to the different microstructures of the alloys. While in the Fe-10Mn6Si1Pd alloy atoms are arranged in a single crystal structure (the body-centered cubic crystal structure of Fe with Mn atoms occupying

substitutional positions), in the Fe-30Mn6Si1Pd alloy two crystal structures (a face-centered cubic and a hexagonal structure) coexist. Hence, different corrosion/degradation characteristics are expected between both alloys.

### **3.2. Evolution of magnetic and mechanical properties**

The magnetic behavior of both alloys before and after immersion is compared in Figure 6. In the as-cast state the alloy with 10% Mn is ferromagnetic, as it is mainly composed of ferrite phase. On the contrary, the alloy with 30% Mn is mainly paramagnetic as a result of the non-magnetic nature of the  $\gamma$ -austenite and  $\epsilon$ -martensite phases.

After immersion, the magnetization of the ferromagnetic Fe-10Mn6Si1Pd alloy remains almost unaltered, while the coercivity decreases slightly. Conversely, the Fe-30Mn6Si1Pd alloy does not become ferromagnetic after immersion in Hank's solution. In view of these magnetic properties, these two alloys could find different applications in the biomedical field. While the Fe-10Mn6Si1Pd alloy could be used as building block in magnetically (wirelessly)-actuated microrobots (e.g., for drug delivery),<sup>27,28</sup> the Fe-30Mn6Si1Pd alloy would be more appropriate to be used as an orthopaedic implant because its non-magnetic character would make it compatible with NMR and MRI analyses.

The mechanical properties of the as-cast and immersed alloys were measured by nanoindentation. Compression tests were also performed on the as-cast materials. Note that the purpose of carrying out nanoindentation in the alloys after immersion was to capture the mechanical properties of the corrosion layers formed in the course of immersion tests rather than to study the overall mechanical behavior of the alloys.

Figure 6S shows the typical load-unload curves of the Fe-10Mn6Si1Pd and Fe-30Mn6Si1Pd alloys after 1-month immersion. For this particular case, the maximum penetration depth is 2.2  $\mu\text{m}$  for the alloy with 10 % Mn and 2.8  $\mu\text{m}$  for the alloy with 30% Mn. The measurements carried out after 1 month of immersion show that the penetration depth is larger than the thickness limit that is usually considered as necessary in order to avoid the contribution from the substrate or the underlying material in the obtained results (typically, the maximum penetration depth must be lower than 1/10<sup>th</sup> the thickness of the sample<sup>20</sup>). Hence, especially for short-term immersion,  $H$  and  $E_r$  of the oxide layers are influenced by the properties of the bulk material. For longer

immersion times, the oxide layers become thicker and the obtained values of  $H$  and  $E_r$  are thus mainly those of these oxide layers.

The dependences of  $E_r$  and  $H$  for both samples as a function of immersion time are presented in Figure 7. Both in the as-cast condition and after immersion, the Fe-10Mn6Si1Pd alloy exhibits larger hardness than the Fe-30Mn6Si1Pd alloy. Since Mn is mechanically harder than Fe, the different  $H$  values in the as-cast state are probably due to the dissimilar crystallographic phases that constitute these alloys. Namely, the presence of austenite (mechanically softer phase) probably contributes to the observed lower hardness in the Fe-30Mn6Si1Pd alloy.

Compression tests performed on the as-cast alloys (see Fig. 7S from the S.I.) shed further light on the mechanical behavior of these quaternary alloys. The stress-strain curves reveal that these alloys exhibit work-hardening behavior, which is particularly noticeable for the Fe-30Mn6Si1Pd material. Such work hardening has been reported in the literature in binary Fe-30Mn alloy,<sup>29,30</sup> Fe-Mn-Si<sup>13</sup> or Fe-Mn-C,<sup>30</sup> and is generally ascribed to a deformation-induced martensitic transformation and/or accumulation of dislocations and mechanical twinning. Under the action of mechanical stress, austenite tends to transform to martensite, resulting in pronounced plasticity (larger than 40% for the Fe-30Mn6Si1Pd). The Young's modulus values determined from compression tests are 50.3 GPa for Fe-10Mn6Si1Pd and 59.7 GPa for Fe-30Mn6Si1Pd. The yield stress values are approximately 650 MPa and 270 MPa, respectively. These values are in good agreement with similar alloys from the literature.<sup>13,30,31</sup> It should be noted that the Young's moduli obtained from nanoindentation are larger than those from compression tests. Similarly, the yield stress ( $\sigma_y$ ) that would be determined from nanoindentation using a constraint factor equal to 3 (i.e.,  $H = 3 \sigma_y$ ) is much larger than the  $\sigma_y$  values from compression tests. These effects can be understood as a direct consequence of the work hardening behavior. Namely, while  $E$  and  $\sigma_y$  from compression tests are obtained in the purely elastic regime (i.e., before work hardening has occurred), the values of  $E_r$  and  $H$  from nanoindentation are obtained after both, plastic and elastic, deformations have occurred. In other words, the values of  $H$  and  $E_r$  from nanoindentation are already influenced by the work-hardening that occurs in the investigated alloys during the course of nanoindentation tests.

As shown in Figure 7, in both alloys,  $H$  and  $E_r$  progressively decrease with the immersion time. The formation of surface oxides cannot explain this result by itself, since usually oxide

materials are mechanically harder and exhibit higher Young's modulus than metallic alloys. However, as already discussed, these oxide layers are not flat and smooth. Actually, they tend to show a particulate and porous surface appearance (see inset in Figure 7a). The occurrence of surface roughness and porosity is known to reduce both  $H$  and  $E_r$ .<sup>4</sup> Remarkably,  $E_r$  of both alloys reaches values close to 20 GPa after long-term immersion, a value which is close to the Young's modulus of human bones (3–27 GPa), hence favoring good biomechanical compatibility between an eventual implant and the neighboring bone tissue.<sup>32</sup> The dissimilar surface porosity between the two investigated alloys can also contribute to the different values of hardness after long-term immersion, besides the aforementioned role of the crystallographic phases constituting the two systems.

### 3.3. Corrosion Behavior

The potentiodynamic polarization curves obtained for the Fe-10Mn6Si1Pd and Fe-30Mn6Si1Pd in Hank's solution are illustrated in Figure 8. For comparison purposes, the potentiodynamic polarization curve of Fe-30Mn-6Si is also provided. The three alloys showed a similar profile; namely, they underwent rapid corrosion immediately after the  $E_{\text{corr}}$  values were surpassed pointing to a uniform corrosion mechanism, probably related to metal dissolution. At approximately 0.5 V vs. Ag/AgCl  $j_{\text{corr}}$  stabilized. This passive region could be ascribed to the protective/blocking effect impaired by the oxide layers formed onto the alloy.  $E_{\text{corr}}$  for the Fe-10Mn6Si1Pd alloy is shifted towards more positive values compared to the quaternary alloy with 30 wt.% Mn, reflecting the different chemical composition of the material and suggesting a delayed onset of material corrosion.

The potentiodynamic curve of the control ternary alloy exhibits a corrosion potential ( $E_{\text{corr}}$ ) of 0.70 V. This value is slightly more positive than that of the quaternary alloy with 10% of Mn ( $E_{\text{corr}} = 0.63$  V) but lower than that of the quaternary alloy with 30 % of Mn ( $E_{\text{corr}} = 0.77$  V). Therefore, it seems that the addition of 1 % of Pd to the ternary Fe-30Mn6Si alloy does trigger the onset of corrosion. It is difficult to draw meaningful conclusions regarding the corrosion rate based on the electrochemical polarization curves. Nevertheless, Liu et al.<sup>13</sup> demonstrated that the Fe-30Mn6Si alloy exhibits higher corrosion rate than both Fe30Mn and pure iron. Previous ICP results (Figure 5) indicate that for short immersion times (7 and 30 days) the total amount of ions

released is slightly larger for the alloy with 30 % Mn. After long-term immersion, though, the alloy with 10% Mn degrades considerably more than the alloy with 30% Mn. This suggests that the oxide layer formed onto the Fe-30Mn6Si1Pd alloy is more compact, which further hinders ion release to some extent and slows down biodegradation. Indeed, cross-section SEM analyses (Figure 4) indicate that the oxide layer for the Fe-10Mn6Si1Pd alloy is much thinner and discontinuous. Even though both potentiodynamic polarization curves are very similar, the lower corrosion potential and the less pronounced slope of the initial part of the anodic branch for the quaternary alloy with 30 % of Mn might explain the different behavior observed between both alloys during the degradation experiments; however, for longer immersion periods similar degradation/corrosion is expected for both quaternary compositions.

### **3.4. Wettability**

Contact angle measurements assessed in Hank's solution medium are presented in Figure 9. The alloy with 30 % Mn exhibits slightly higher contact angle ( $82 \pm 4^\circ$ ) than the alloy with 10% Mn ( $67 \pm 6^\circ$ ). Typically, the contact angle value can be regarded as a parameter indicative of adhesion properties: smaller contact angles indicate better adhesion properties. Materials that exhibit contact angles larger than  $90^\circ$  are hydrophobic and are expected to exhibit poorer cell adhesion.<sup>33</sup> Consequently, the lower wetting angle measured in the Fe-10Mn6Si1Pd alloy compared to that observed in the Fe-30Mn6Si1Pd alloy may be indicative of improved cell adhesion for this alloy in the as-cast state.

### **3.5. Biocompatibility**

Concerning alloys biocompatibility, two different types of analyses were performed: cytotoxicity and cell proliferation. Cytotoxicity analysis allows determining whether the alloy produces a cytotoxic effect (i.e., a decrease in the live cell number with time), whereas cell proliferation analysis allows to assess whether cells growing on the alloy can proliferate (i.e., increase their number over time).

Live/Dead kit was used to determine cytotoxicity at different time intervals on each composition. As shown in Figure 10(a-f), after cell culturing for 1 day, the number of Saos-2 cells attached to the surface of Fe-10Mn6Si1Pd was higher than for Fe-30Mn6Si1Pd. This result

is in agreement with the lower contact angle measured for the Fe-10Mn6Si1Pd (Figure 9), which favors cell adhesion. Indeed, previous studies have reported that 64° contact angles allowed an optimal cell adhesion compared with 90° contact angles, considered as hydrophobic surfaces.<sup>34</sup> The number of live cells after one day in culture was higher than 90% in both cases. However, after 3 and 7 days of culture, the results were reversed: the number of live cells on Fe-10Mn6Si1Pd was dramatically reduced, whereas it increased for cells cultured on the Fe-30Mn6Si1Pd alloy. Finally, after 40 days in culture very few cells remained attached to the surface of the Fe-10Mn6Si1Pd alloy, but the surface of Fe-30Mn6Si1Pd was still covered with a monolayer of live Saos-2 cells.

The results of Saos-2 cells proliferation can be seen in Figure 10g. After one day in culture, the fluorescence intensity of live cells on the Fe-10Mn6Si1Pd alloy was more than three times the value of cells on the Fe-30Mn6Si1Pd alloy. However, the total cell number on the Fe-10Mn6Si1Pd alloy decreased with time, becoming almost null after 60 days, while for the Fe-30Mn6Si1Pd alloy it progressively increased with culture time.

One possible explanation for the observed trend in cell viability and proliferation on the two alloys could be the pronounced degradation of the Fe-10Mn6Si1Pd alloy that occurs upon immersion. However, the ICP analyses carried out following the ASTM-G31-72 norm (Figure 5) did not evidence pronounced ion release during the first 30 days of immersion. Probably, the large volume of Hank's solution used precludes a clear detection, by ICP, of the alloys' dissolution during the first days of immersion, in spite of the obvious formation of a corrosion oxide layer after a few weeks inside the Hank's solution (Figures 2 and 3). To better understand the cytotoxicity of the two alloys, ICP analyses were also carried out on droplets extracted from the small volumes of DMEM with 10% FBS required for the cell culture assays. Figure 11 reveals that in such concentrated conditions, pronounced ion release takes place from the very few days of immersion and, as expected, the Fe-10Mn6Si1Pd alloy degrades much faster than the Fe-30Mn6Si1Pd one, in agreement with Figure 5. The pronounced ion release, together with the poor adhesion of the corrosion oxide layer in the Fe-10Mn6Si1Pd alloy (Figures 2 and 3), probably account for the progressive decrease of live cells in this particular material.

Regarding cell morphology, SEM analysis of Saos-2 cells grown on alloy surfaces showed differences in shape and spreading between compositions and time intervals (Figure 12). After



24 h in culture, cells observed on top of the Fe-10Mn6Si1Pd alloy presented a flattened and polygonal morphology with membrane projections. However, after 3 days in culture, a decrease in the number of cells was observed, and those still remaining on the alloy were no longer completely adhered to the surface. They were round in shape, a sign of the difficulty for the cells to remain attached. Conversely, although a relatively small amount of cells were attached to the surface of the Fe-30Mn6Si1Pd alloy after 1 day, some of them were well adhered, with fusiform and flattened shapes. In this case, the number of well-spread cells increased with time, achieving a monolayer of cells after long-term culture.

Altogether, the results indicate a completely different behavior of the cells on top of both alloys. Cells initially adhered more easily onto the Fe-10Mn6Si1Pd alloy than on the Fe-30Mn6Si1Pd one, as expected by the higher hydrophilicity of Fe-10Mn6Si1Pd surface.<sup>34</sup> But, eventually, the ions and debris released into the medium due to the degradation of the Fe-10Mn6Si1Pd alloy produced a negative effect on the cells, resulting in their detachment and subsequent death. Contrarily, the few cells that were able to attach to the Fe-30Mn6Si1Pd alloy surface were able to remain adhered over time and proliferate. This is in accordance with the SEM images of the 30% Mn alloy after 1 month of immersion in Hank's solution, which showed that the surface of the alloy was completely covered with a well-adhered and considerably smooth oxide layer which, in turn, hinders ion release and degradation. On the contrary, the alloy with 10% Mn exhibited a cracked and loose oxide layer, which facilitates ion release, hence hampering cell proliferation on the alloy's surface. Indirect studies performed with Fe-10Mn6Si1Pd alloy showed that cytotoxicity was not increased in cells growing in presence of this alloy but not in direct contact with it (see Fig. 8S in the S.I.). This confirms that the material is not cytotoxic by itself but the cracking and oxide formation in the surface hinders cell adhesion. Adhesion is mandatory for all adherent cells, as is the case of Saos-2 cell; when cells cannot adhere, they die.

### **3.6. Hemolysis**

The HR of Fe-10Mn6Si1Pd and Fe-30Mn6Si1Pd were 1.6 and 0.7, respectively. Both values were lower than 5%, indicating that both alloys are non-hemolytic, according to the Standard

Practice for Assessment of Hemolytic Properties of Materials (ASTM-F756-08). Thus, both alloys could be good candidates for bioimplant devices.

#### 4. Conclusions

1. Structural analyses reveal that the Fe-30Mn6Si1Pd alloy consists of  $\epsilon$ -martensite,  $\gamma$ -austenite and homogeneously dispersed Pd-rich precipitates, while the Fe-10Mn6Si1Pd alloy contains  $\alpha$ -ferrite and Pd-rich precipitates. In the as-cast condition, good mechanical response was observed by nanoindentation: hardness values of 5.6 GPa and 4.2 GPa, and reduced Young's modulus of 125.2 GPa and 93.1 GPa were measured for the Fe-10Mn6Si1Pd and Fe-30Mn6Si1Pd alloys, respectively, by nanoindentation. Work hardening behavior was observed during compression tests, with total strain values exceeding 30% in both alloys.
2. Contrary to the ferromagnetic response of the Fe-10Mn6Si1Pd alloy, the paramagnetic Fe-30Mn6Si1Pd alloy is more appropriate to be used as an implant since it would be compatible with nuclear magnetic resonance and magnetic imaging analyses.
3. A loose oxide layer tends to form with immersion time in the the Fe-10Mn6Si1Pd alloy, whereas the corrosion layer is more robust for Fe-30Mn6Si1Pd alloy. As a consequence, higher ion release concentration is observed for the alloy with 10 % Mn.
4. The formation of rough and porous oxide layers at the surface of the alloys during immersion contributes to decrease the indentation hardness and the reduced Young's modulus with immersion time, while virtually no variations in the overall magnetic properties of both samples are observed.
5. Both Fe-10Mn6Si1Pd and Fe-30Mn6Si1Pd are initially biocompatible. The more hydrophilic character of the Fe-10Mn6Si1Pd alloy (as assessed by wettability tests) favors the initial cell adhesion. However, the formation of a cracked, loosely attached, oxide layer in this case, facilitates a pronounced ion release, hence hampering cell proliferation on the surface of this alloy, as compared to Fe-30Mn6Si1Pd.

6. Overall, the Fe-30Mn6Si1Pd alloy is a promising candidate for biodegradable implant applications since it combines a non-magnetic character with good Saos-2 cell proliferation.

## **Acknowledgments**

This work has been partially funded by the 2014-SGR-1015 project from the Generalitat de Catalunya, and the MAT2014-57960-C3-1-R (co-financed by the *Fondo Europeo de Desarrollo Regional*, FEDER), the MAT2014-57960-C3-2-R and MAT2014-57960-C3-3-R projects from the Spanish *Ministerio de Economía y Competitividad* (MINECO). Dr. Eva Pellicer is grateful to MINECO for the “Ramon y Cajal” contract (RYC-2012-10839).

## References

- 1 Y. H. Yun, Z. Y. Dong, N. Lee, Y. J. Liu, D. C. Xue, X. F. Guo, J. Kuhlmann, A. Doepke, H. B. Halsall, W. Heineman, S. Sundaramurthy, M. J. Schulz, Z. Z. Yin, V. Shanov, D. Hurd, P. Nagy, W. F. Li and C. Fox, *Mater Today*, 2009, **12**, 22.
- 2 B. Zberg, P. J. Uggowitzer and J. F. Loffler, *Nat Mater*, 2009, **8**, 887.
- 3 M. Schinhammer, A. C. Hanzi, J. F. Loffler and P. J. Uggowitzer, *Acta Biomater*, 2010, **6**, 1705.
- 4 E. Pellicer, S. Gonzalez, A. Blanquer, S. Surinach, M. D. Baro, L. Barrios, E. Ibanez, C. Nogues and J. Sort, *J Biomed Mater Res A*, 2013, **101**, 502.
- 5 Y. Ding, Y. Li, J. Lin and C. Wen, *J Mater Chem B*, 2015, **3**, 3741.
- 6 J. Kubasek, D. Vojtech, J. Lipov and T. Ruml, *Mat Sci Eng C-Mater*, 2013, **33**, 2421.
- 7 M. Peuster, C. Hesse, T. Schloo, C. Fink, P. Beerbaum and C. von Schnakenburg, *Biomaterials*, 2006, **27**, 4955.
- 8 R. Waksman, R. Pakala, R. Baffour, R. Seabron, D. Hellinga and F. O. Tio, *J Interv Cardiol*, 2008, **21**, 15.
- 9 F. Moszner, A. S. Sologubenko, M. Schinhammer, C. Lerchbacher, A. C. Hanzi, H. Leitner, P. J. Uggowitzer and J. F. Loffler, *Acta Mater*, 2011, **59**, 981.
- 10 M. Schinhammer, C. M. Pecnik, F. Rechberger, A. C. Hanzi, J. F. Loffler and P. J. Uggowitzer, *Acta Mater*, 2012, **60**, 2746.
- 11 H. Hermawan, H. Alamdari, D. Mantovani and D. Dube, *Powder Metall*, 2008, **51**, 38-45.
- 12 H. Hermawan, D. Dube and D. Mantovani, *J Biomed Mater Res A*, 2010, **93A**, 1.
- 13 B. Liu, Y. F. Zheng and L. Q. Ruan, *Mater Lett*, 2011, **65**, 540.
- 14 Z. G. Xu, M. A. Hodgson and P. Cao, *Mat Sci Eng A-Struct*, 2015, **630**, 116.
- 15 S. N. Balo, *J Supercond Nov Magn*, 2013, **26**, 1085.
- 16 ASTM Standard G31-72, *Standard Practice for Laboratory Immersion Corrosion Testing of Metals*, ASTM Standards, Philadelphia, PA, USA, 2004
- 17 L. Petrini, F. Migilavacca, *Journal of Metallurgy*, 2011, **2011**, 501483
- 18 H. Hermawan, A. Purnama, D. Dube, J. Couet, D. Mantovani, *Acta Biomater*, 2010, **6**, 1852.

- 19 M. Moravej, A. Purnama, M. Fiset, J. Couet and D. Mantovani, *Acta Biomater*, 2010, **6**, 1843.
- 20 W. C. Oliver and G. M. Pharr, *J Mater Res*, 1992, **7**, 1564.
- 21 J. Fornell, E. Pellicer, N. Van Steenberge, S. Gonzalez, A. Gebert, S. Surinach, M. D. Baro and J. Sort, *Mat Sci Eng A-Struct*, 2013, **559**, 159.
- 22 B. H. Jiang, T. Tadaki, H. Mori and T. Y. Hsu, *Mater T JIM*, 1997, **38**, 1072.
- 23 I. P. Spiridon, N. M. Lohan, M. G. Suru, E. Mihalache, L. G. Bujoreanu and B. Pricop, *Met Sci Heat Treat*, 2016, **57**, 548.
- 24 M. Schinhammer, P. Steiger, F. Moszner, J. F. Loffler and P. J. Uggowitzer, *Mat Sci Eng C-Mater*, 2013, **33**, 1882.
- 25 M. Schinhammer, I. Gerber, A. C. Hanzi and P. J. Uggowitzer, *Mat Sci Eng C-Mater*, 2013, **33**, 782.
- 26 W.M. Haynes, *Handbook of Chemistry and Physics, 94th Edition*, CRC Press, 2013.
- 27 S. Schuerle, S. Pane, E. Pellicer, J. Sort, M. D. Baro and B. J. Nelson, *Small*, 2012, **8**, 1498.
- 28 M. A. Zeeshan, S. Pane, S. K. Youn, E. Pellicer, S. Schuerle, J. Sort, S. Fusco, A. M. Lindo, H. G. Park and B. J. Nelson, *Adv Funct Mater*, 2013, **23**, 823.
- 29 X. Liang, J.R. McDermid, O. Bouaziz, X. Wang, J.D. Embury, H.S. Zurob, *Acta Mater*, 2009, **57**, 3978.
- 30 X. Wang, H.S. Zurob, J.D. Embury, X. Ren, I. Yakubtsov, *Mat Sci Eng A*, 2010, **527**, 3785.
- 31 A. Francis, Y. Yang, S. Virtanen, A.R. Boccaccini, *J Mater Sci: Mater Med*, 2015, **26**, 138.
- 32 X. N. Gu, Y. F. Zheng, S. P. Zhong, T. F. Xi, J. Q. Wang and W. H. Wang, *Biomaterials*, 2010, **31**, 1093.
- 33 J. H. Wei, T. Igarashi, N. Okumori, T. Igarashi, T. Maetani, B. L. Liu and M. Yoshinari, *Biomed Mater*, 2009, **4**, 045002.
- 34 D. P. Dowling, I. S. Miller, M. Ardhaoui and W. M. Gallagher, *J Biomater Appl*, 2011, **26**, 327.

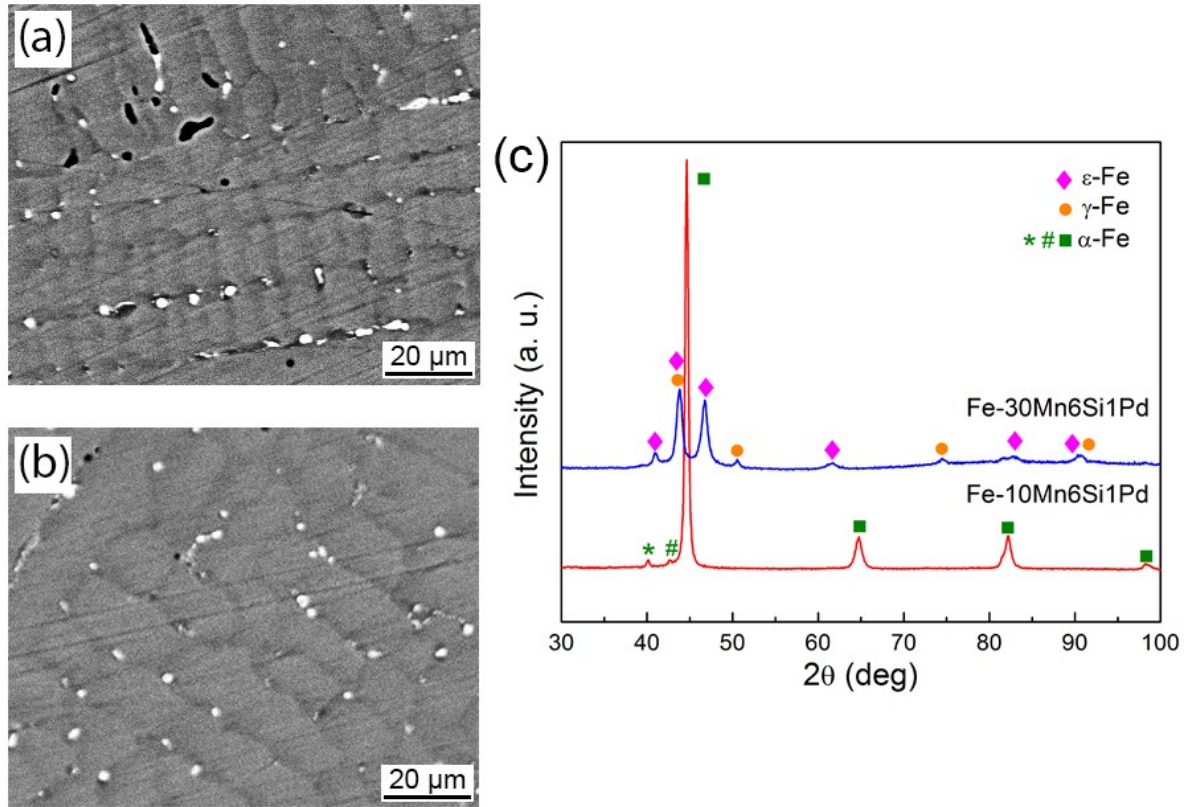


**Fig. 1:** SEM images of (a) Fe-10Mn6Si1Pd and (b) Fe-30Mn6Si1Pd polished alloys. (c) XRD patterns of as-cast Fe-10Mn6Si1Pd and Fe-30Mn6Si1Pd alloys. Note that the small peaks denoted with \* and # belong to the  $\alpha$ -Fe phase and come from the  $K_{\beta}$  and  $W L_{\alpha}$  reflections, respectively. The other peaks come from the  $K_{\alpha}$  radiation.

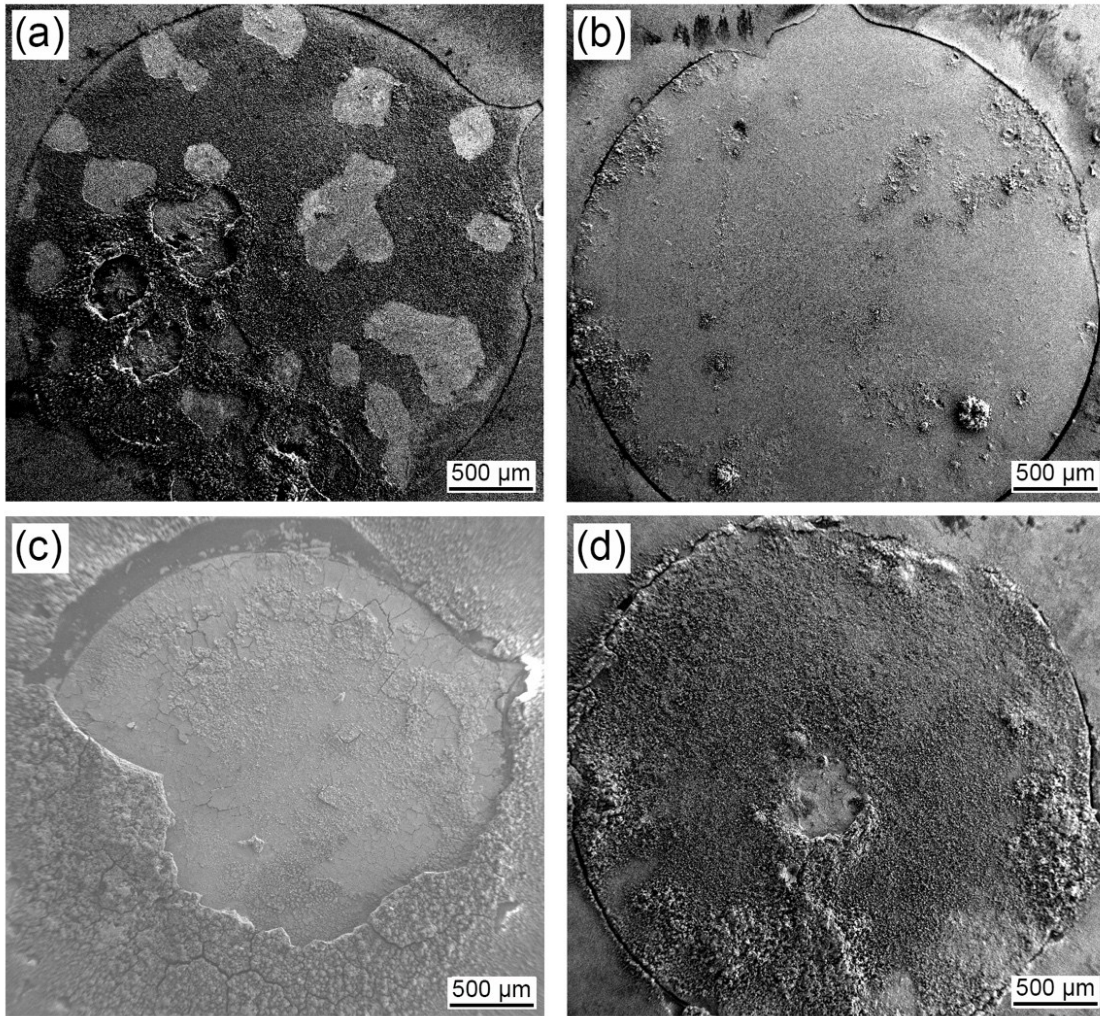


**Fig. 2:** Low magnification SEM micrographs of: (a,c) Fe-10Mn6Si1Pd alloy after immersion in Hank's solution [for (a) 1 month and (c) 4 months], and (b,d) Fe-30Mn6Si1Pd alloy after immersion for (b) 1 month and (d) 4 months.

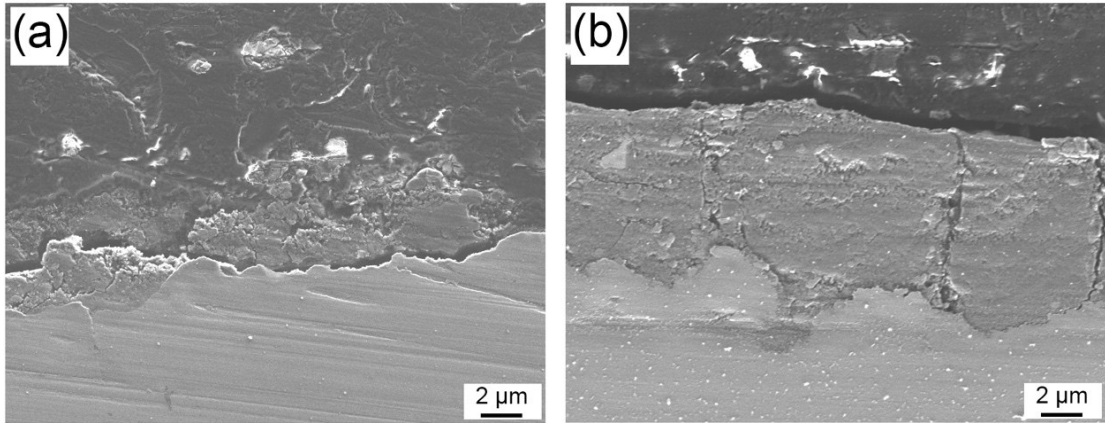


**Fig. 3:** Cross section SEM images of (a) Fe-10Mn6Si1Pd and (b) Fe-30Mn6Si1Pd alloys after 1 month of immersion in Hank's solution.

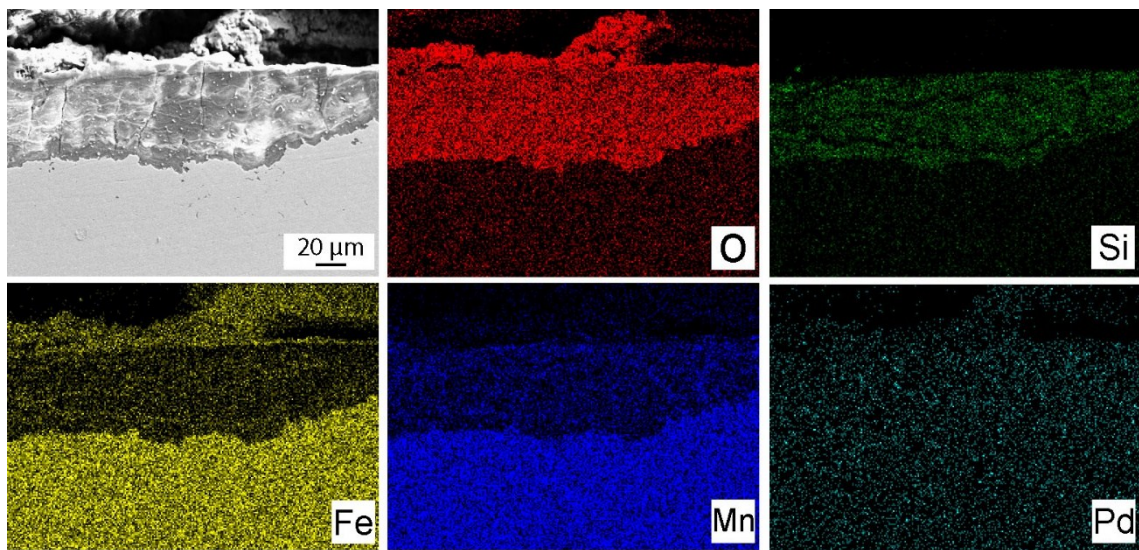


**Fig. 4:** Cross section SEM images of Fe-30Mn6Si1Pd after immersion in Hank's solution for 4 months together with the element distributions of O, Si, Fe, Mn and Pd.



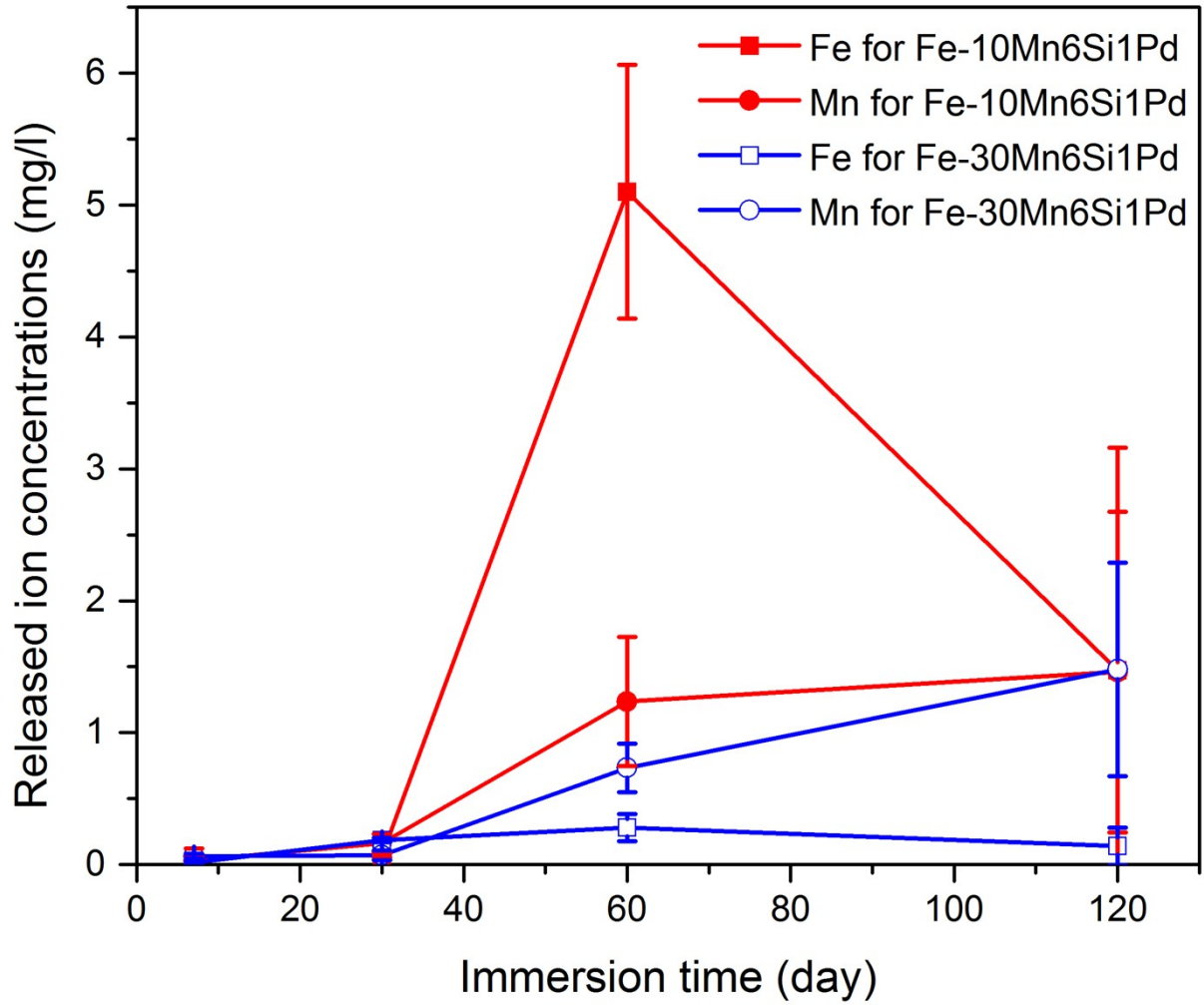


**Fig. 5:** ICP ions release concentrations of Fe-10Mn6Si1Pd and Fe-30Mn6Si1Pd alloys as a function of immersion time in Hank's solution, carried out in accordance with the ASTM-G31-72 norm, i.e., using a large volume of Hank's solution (see text for details).

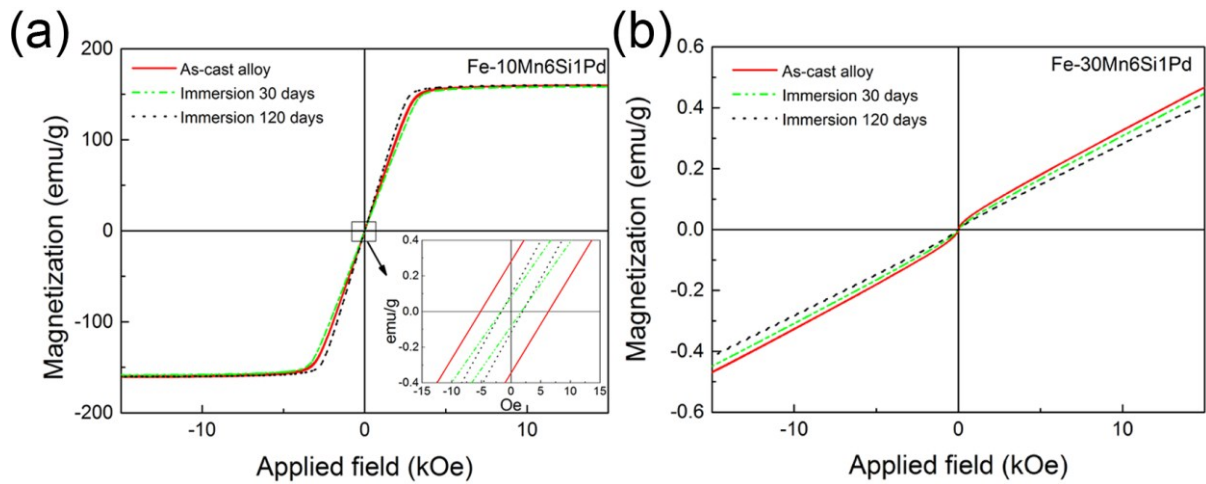


**Fig. 6:** Dependence of the magnetization as a function of applied magnetic field for Fe-10Mn6Si1Pd and Fe-30Mn6Si1Pd as a function of immersion time

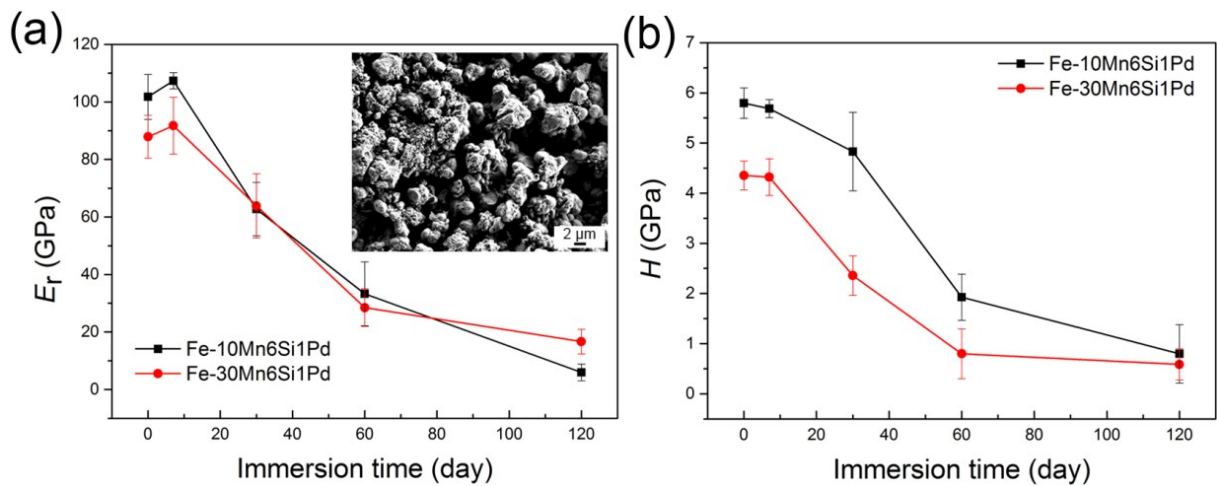


**Fig. 7:** Dependence of the reduced Young's modulus ( $E_r$ ) and hardness ( $H$ ) for Fe-10Mn6Si1Pd and Fe-30Mn6Si1Pd as a function of immersion time. The inset in (a) shows an on-top high-resolution SEM image of the corrosion oxide layer corresponding to the Fe-30Mn6Si1Pd after immersion for 120 days, where it can be seen that it shows a rather particulate and porous morphology.

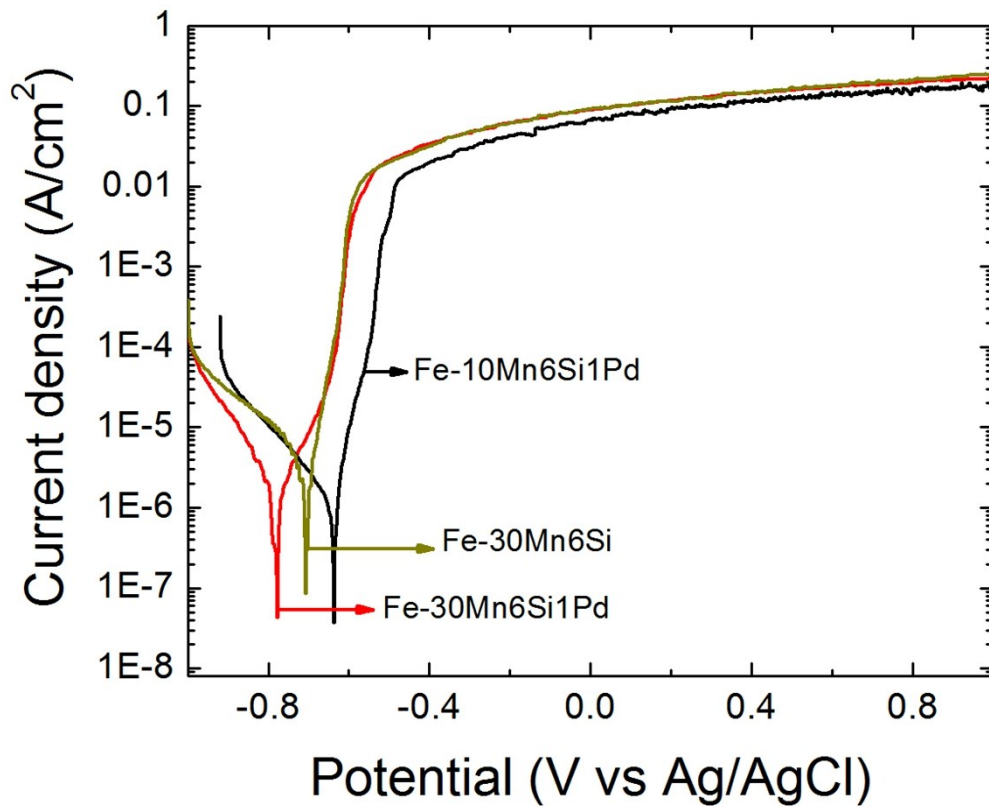


**Fig. 8:** Potentiodynamic polarization curves corresponding to the two quaternary Fe-based alloys, as well as the ternary Fe-30Mn6Si (for the sake of comparison), in Hank's solution at 37 °C.

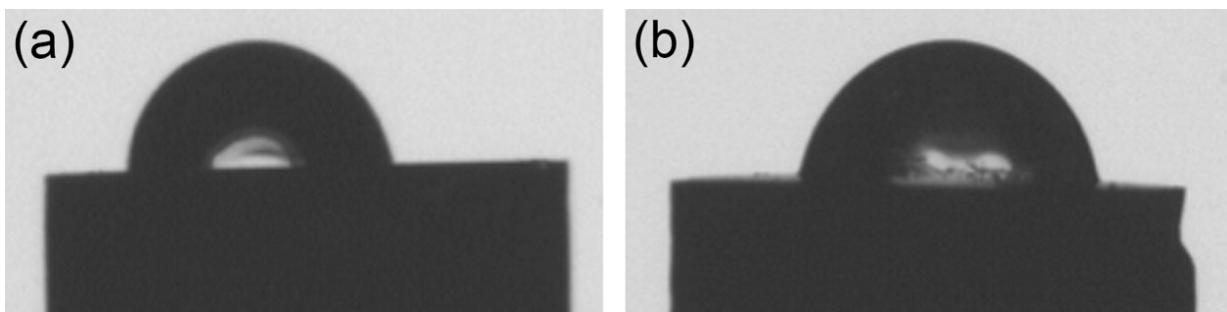


**Fig. 9:** Contact angle measurements for (a) Fe-10Mn6Si1Pd and (b) Fe-30Mn6Si1Pd, both assessed in Hank's solution medium.

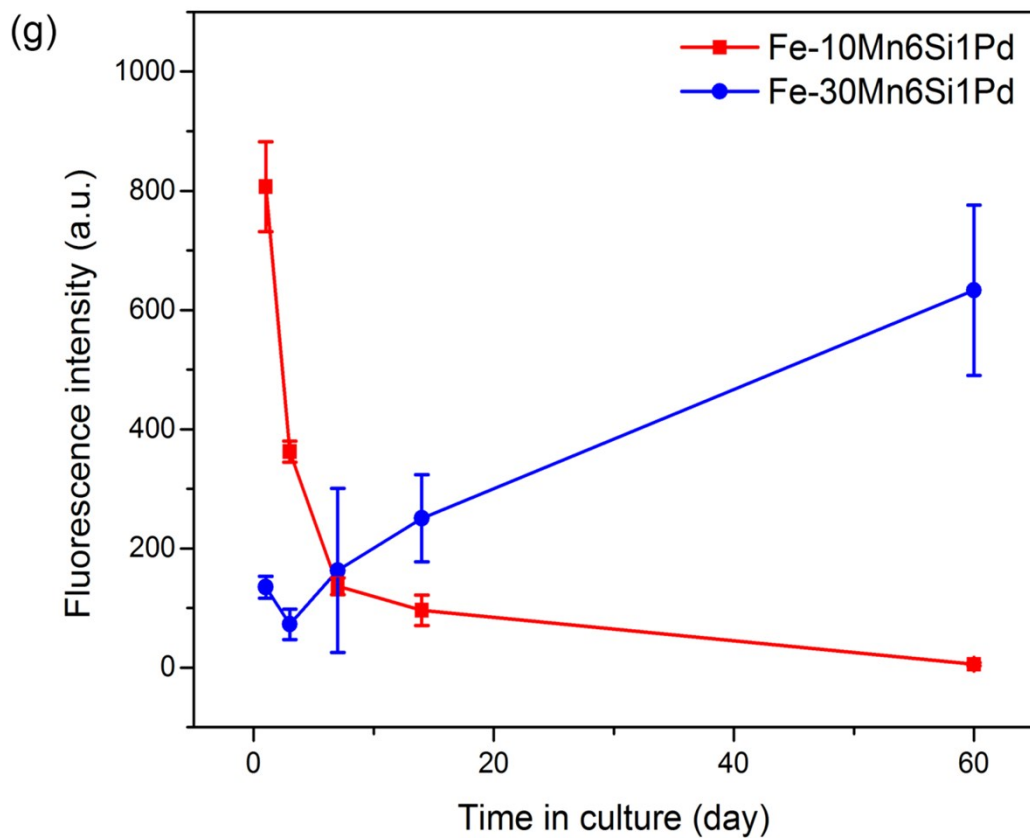
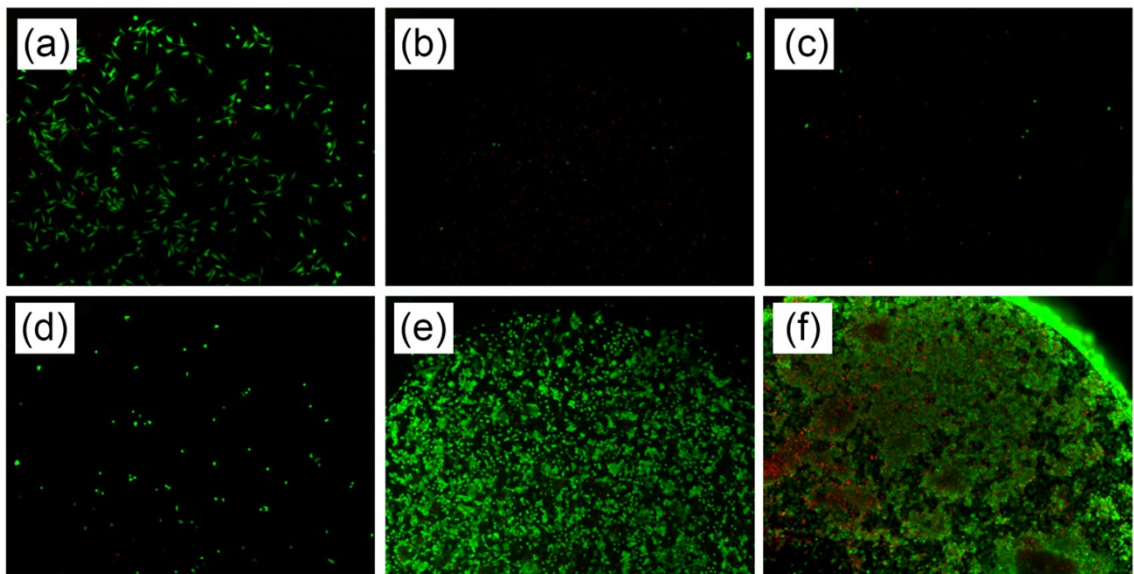


**Fig. 10:** Saos-2 cells cultured onto Fe-10MnSiPd and Fe-30MnSiPd alloys. Cell viability on (a-c) Fe-10MnSiPd and (d-f) Fe-30MnSiPd alloys at: (a,d) 1 day, (b,e) 7 days and (c-f) 40 days. Live cells stained in green and dead cells stained in red on. (g) Saos-2 cell proliferation on both alloy surfaces measured by Alamar Blue fluorescence at 1, 3, 7, 14 and 60 days.

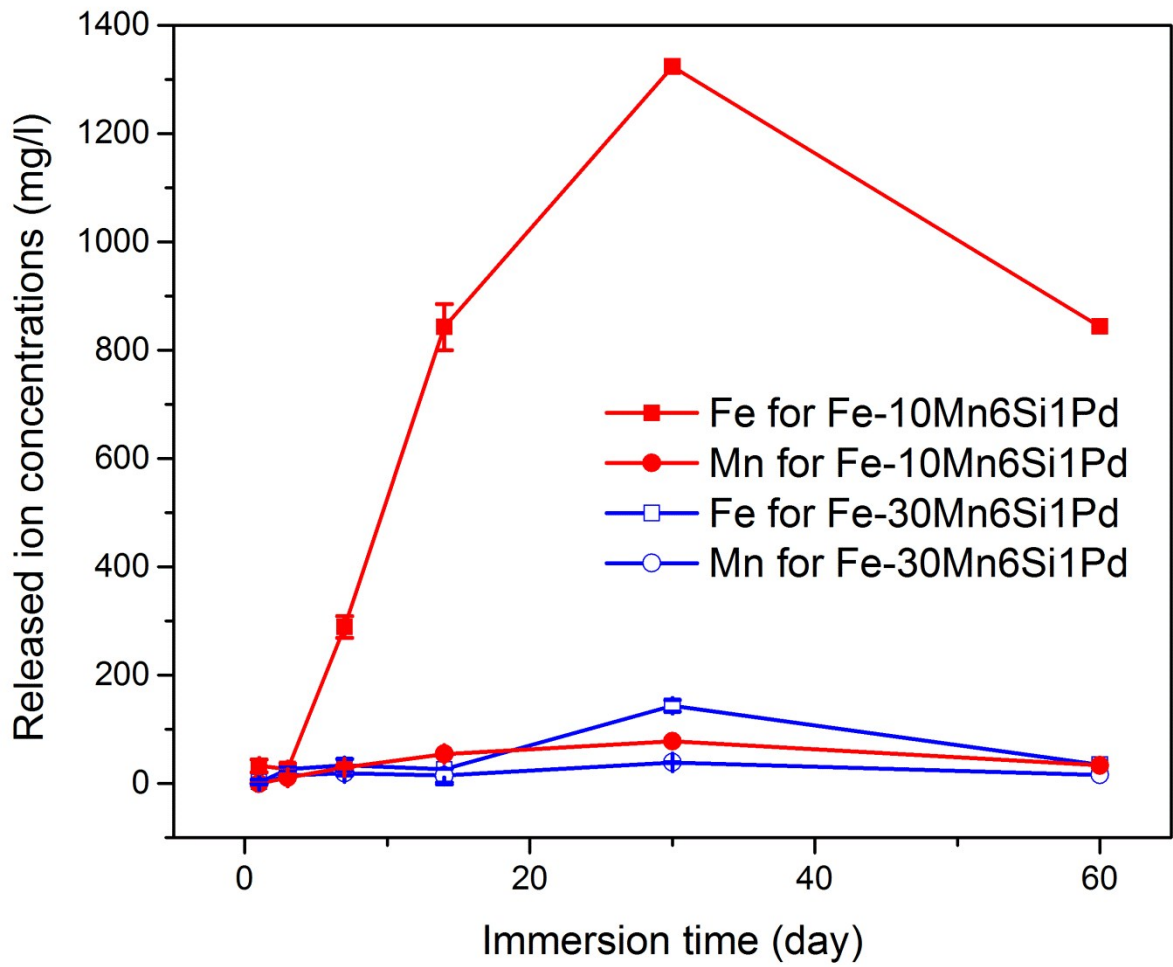


**Fig. 11:** Evolution of the ICP ions release concentrations of Fe-10Mn6Si1Pd and Fe-30Mn6Si1Pd alloys as a function of immersion time in Hank's solution for the same conditions used in the biological tests, i.e. with a small volume of solution (see text for details).

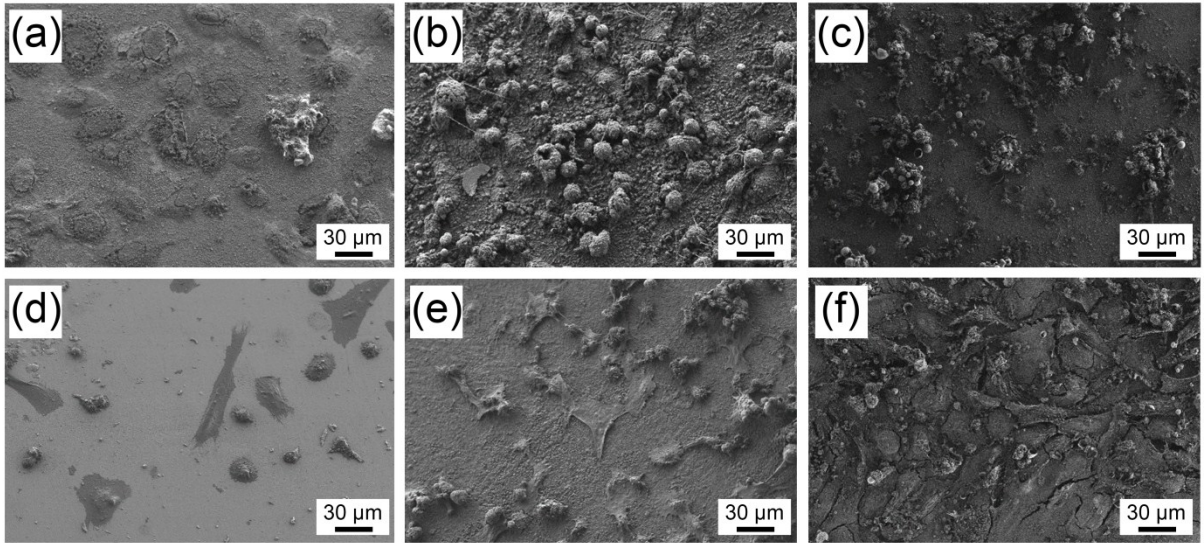


**Fig. 12:** SEM images of Saos-2 cells grown on (a-c) Fe-10MnSiPd and (d-f) Fe-30MnSiPd after (a,d) 1 day, (b,e) 3 days and (c,f) 7 days.